

Shadows of generalised Hayward spacetimes : in vacuum and with plasma

Suvikranth Gera,¹ Saurabh Kumar,^{2,3} Poulami Dutta Roy,³ and Sayan Chakrabarti²

¹*Department of Physics, IIT Guwahati, Guwahati, Assam, India.**

²*Department of Physics, IIT Guwahati, Guwahati, Assam, India.*

³*Chennai Mathematical Institute, Siruseri 603103, Tamil Nadu, India[†]*

Abstract

The Hayward regular BH solution attempted to resolve the curvature singularity issue by entering the domain of non-singular spacetimes. Recently, Dutta Roy and Kar (Phys. Rev. D 106, 044028) expanded this solution to encompass a broader range of spacetimes. These spacetimes are constructed based on the Damour-Solodukhin prescription, which involves introducing different metric parameters in the g_{tt} and g_{rr} components of the original Hayward line element, and are characterized by two parameters (σ, κ) . This generalization gives rise to both known and novel regular/singular BHs as well as various types of wormhole spacetimes. In this work, we explore the spacetimes that emerge for different values of (σ, κ) from the generalized Hayward metric, particularly focusing on their shadows in vacuum and when surrounded by plasma. Intriguingly, we observe the presence of both photon and anti-photon spheres for certain regular spacetimes. Our study highlights the differences in the shadows of different types of regular spacetime compared to those of the singular BH derived from the generalized Hayward metric and also sheds light on the impact of plasma on the shadow radius.

* suvikranth@iitg.ac.in

† ksaurabhkumar.712@gmail.com

I. INTRODUCTION

The theory of general relativity (GR), with black holes (BH) as one of the solutions, is widely regarded as the most successful theory of gravity. Until recently, observational tests of GR were predominantly based on probing the weak field limit of gravity [1]. The era of testing GR in the regime of strong gravity and hence the existence of BHs started with the discovery of gravitational waves [2] by the LIGO-Virgo-KAGRA collaboration and simultaneously with the first detection of the shadow of the supermassive BH in M87 galaxy by the Event Horizon Telescope (EHT) collaboration [3]. Despite the success of GR, it is plagued with problems: the existence of curvature singularity, issues with quantization of gravity, are a few among them. To tackle the issue of curvature singularity in GR, a possible solution exists in literature, that of non-singular spacetimes. These regular classes of solutions can be broadly divided into spacetimes with and without horizon like the regular BHs and wormholes, respectively. However, upon a closer inspection of these solutions, one realizes that the issue of singularity is traded for other issues, such as energy condition violating matter for wormholes [4, 5] or mass-inflation instabilities in regular BHs [6–9], provided that these solutions are viewed in the context of GR. While there exists multiple works which show the existence of wormholes in alternative theories of gravity without the need of ‘exotic’ matter [10–22] and possible ways of taming the mass-inflation instability of regular BHs [23, 24], the issues still remains to be conclusively addressed.

BHs are ubiquitous in physics, and at the same time they are the simplest objects in GR. For this reason they are often termed as the hydrogen atom of GR. The simplistic nature of the BHs, along with their extreme gravitational fields, make them the perfect testing bed to examine GR at strong field regimes. Towards this direction, the EHT collaboration has drawn much attention, and shifted the focus of the entire observational community with its first observations via the Very Long Baseline Interferometry (VLBI) of the supermassive BHs at the centers of the galaxies M87 [3] and Sgr A^* [25]. Interestingly, it is to be noted that the EHT observations have achieved the required frequency to resolve the horizon-scale emission from the vicinity of the supermassive BHs at the center of the galaxies. As a result, the observed light from these extreme compact objects includes photons whose trajectories near the horizon of the BHs are deviated from their actual travel paths and describes nearly bound spherical orbits around the BH. This humongous achievement was made possible by a global

network of radio telescopes working in parallel to create a virtual earth-sized observatory. By capturing and analyzing the radio waves emitted by the surrounding accretion disk, the EHT has once again provided a confirmation of the theoretical predictions of photon paths within the theory of GR.

Although GR has achieved significant successes, it also faces severe challenges on the theoretical front. One of the most problematic areas in GR is the presence of the singularities at the core of the BH spacetimes, which raises serious question about the credibility of the theory. The issue that GR is ultraviolet (UV)-incomplete is related to this fact. It is therefore proposed that GR requires modifications in the regions where the spacetime curvature becomes high. Such modifications is necessary if one requires a theory of gravity which is UV complete. One potential approach to address the singularity issue is to consider specific types of matter distributions, which will lead to singularity-free BH solutions. Bardeen first proposed the metric for such a nonsingular BH geometry [26]. Later on, by coupling GR with nonlinear electrodynamics (NLED), a plethora of regular BH solutions with electric and magnetic charges were derived [27–34]. Later on, Hayward proposed a static spherically symmetric BH solution in regular space-time [35]. This metric describes an isolated regular four dimensional spherically symmetric spacetime and contains a length scale ℓ , apart from which, there is only one parameter: the mass of the BH. At large distances the metric takes the Schwarzschild form, while at the origin it is regular and has de Sitter form. The distinguishing feature of such a metric is its scaling behaviour, i.e. the scaling transformation of the coordinates, parameters and the metric preserves the form of the metric.

The literature related to shadows of different extreme compact objects including BHs is very rich and because of the present interest in EHT collaboration’s result, there has been a flurry of works in this direction. Here, we briefly mention some of the important works towards the development of the subject. The shadow of the Schwarzschild black hole was first discussed in [36, 37]. Bardeen [38], again, was the first to describe the nature of the shadow cast by a rotating Kerr black hole, consequently it was generalised in the case of a Kerr-Newman BH in [39]. The shadow of the Kerr black hole as well as a Kerr naked singularity was discussed in [40] by introducing two new observables. Going beyond the standard GR solutions of Einstein’s equations, the study of shadows in BHs in other theories had been discussed extensively in the literature, viz. Einstein-Maxwell-Dilaton-Axion black hole [41], Kerr-Taub-NUT black hole [42], shadows of static spherically symmetric and rotating Kerr

BHs in modified gravity (MOG) theory [43], rotating braneworld black hole [44], rotating non-Kerr type BHs [45], BHs in an expanding Universe [46], BHs in dynamical Chern-Simons modified gravity [47] to name a few. For more detailed on the methods and results in calculating shadows, we refer the readers to the existing reviews [48–50]. On the other hand, the study of shadows in regular BH backgrounds has gained considerable interests in recent years. There has been a lot of works done in this direction, see [51–57] for more details.

In our work, we take a pragmatic approach and address the observational aspects of a class of regular spacetime solutions called the generalized Hayward metric recently developed in Dutta Roy and Kar [58], which describes wormholes, regular BH spacetimes along with the singular BH depending on the choice of the metric parameters. The generalized Hayward metric is a perfect testing ground for comparing the shadows of the regular spacetimes to that of the singular BHs. To our knowledge, the present study incorporating different classes of compact objects, eg. regular BHs, wormholes and singular BHs together, is new. Even though studies on each different topics including wormhole shadows (see [59] for details on wormhole shadows and for more references on the topic) have been performed individually, the present approach to study all these under the same umbrella is new. It is known that certain regular spacetimes possess an anti-photon ring along with the usual photon ring. We explore in detail the occurrence of photon/anti-photon rings in all classes of geometries originating from the generalized Hayward metric and probe the capability of the shadow observations to distinguish the regular spacetimes from the singular BH.

It is known that the shadow of a compact object is associated with the photons scattered from the innermost circular null orbits and, hence, is a characteristic of the compact object. However, this holds true assuming the trajectory of these photons are unaffected throughout their journey from the point of emission to the typical asymptotic observer. In a realistic scenario, compact objects are always surrounded by an interstellar medium, which has a non-trivial effect on the photon trajectories. Hence it is natural to incorporate the effects of the environment in the computations of shadow. As a first step to address these issues, we analytically handle the computations of shadow in the presence of a plasma surrounding the compact object. Although our analysis corresponds to a simplified scenario which are different from a real astrophysical environment, these analytic calculations allow us to understand the explicit dependencies of the shadow profile on the metric and plasma

parameters in contrast to numerical simulations.

To this extent, we follow the techniques described in [60] and restrict to non-magnetized cold plasma consisting of two fluids, which are modeled by ions and electrons. The Hamiltonian for the photon trajectories in the presence of plasma in a curved spacetime background has been done at various levels of sophistication. For example, the rigorous derivation of Hamiltonian for magnetized plasma was achieved by Breur and Ehlers in [61, 62]. For a much simpler case of non-magnetized plasma fluids that we are interested in, the same analysis was carried out in [63, 64]. These results were then applied to the photon trajectories in the equatorial plane of Kerr spacetime by Perlick and others in [63, 65–67] and in a general setup in [68].

The rest of the paper is organized as follows. In section II, we briefly discuss the generalized Hayward metric and the spacetimes arising for different metric parameter values. Section III summarizes the computation of the shadow cast by a static spherically symmetric solution. The main results are discussed in Section IV, consisting of the shadow, with and without plasma, for the different spacetimes originating from the generalized Hayward metric. We summarise the conclusions in Section V.

Unless otherwise stated we have used geometrised units $G = c = 1$.

II. REVIEW OF SPACETIMES ORIGINATING FROM GENERALISED HAYWARD METRIC

In this section, we will discuss the structure of the generalized Hayward metric and give a brief recap about the different spacetimes that originate for different parameter values.

The spherically symmetric, static generalized Hayward metric, introduced in [58] is of the form

$$ds^2 = -f_1(r)dt^2 + \frac{dr^2}{f(r)} + r^2(d\theta^2 + \sin^2\theta d\phi^2), \quad (1)$$

where $f_1(r)$ and $f(r)$ are chosen respectively as

$$f_1(r) = 1 - \frac{2M_1 r^2}{r^3 + 2M_1 \ell^2}; \quad f(r) = 1 - \frac{2Mr^2}{r^3 + 2M\ell^2}. \quad (2)$$

It is important to note that for $M_1 = M$, this metric reduces to the Hayward regular BH, with the square of the parameter ℓ being identified with the inverse of the cosmological constant in the small r limit. In fact, the construction of the generalized Hayward metric is motivated

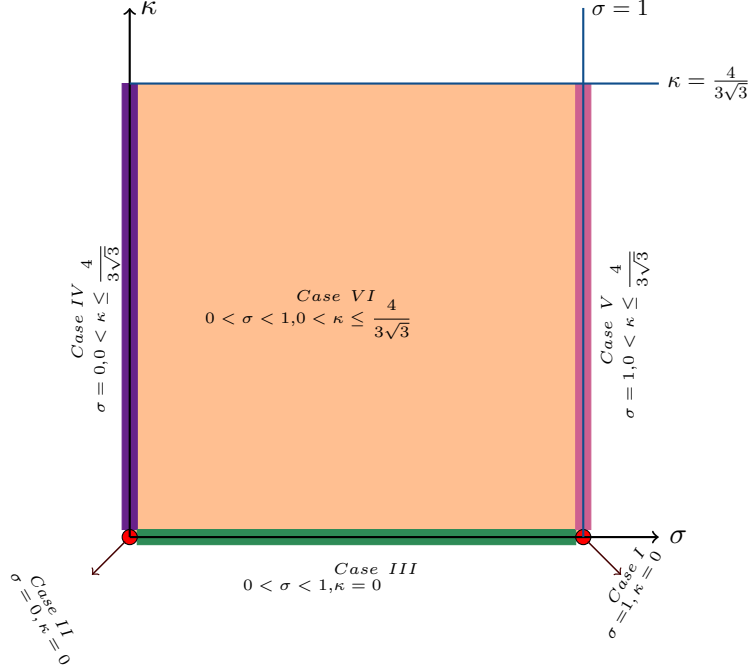


FIG. 1. Parameter space of (σ, κ) showing different spacetimes corresponding to different ranges of the parameters.

from the Hayward BH case by considering two different mass parameters in the g_{tt} and g_{rr} components. The incorporation of a different mass parameter M_1 in the g_{tt} component of the metric, such that $M_1 \neq M$, is inspired by the Damour-Solodukhin wormhole construction based on the Schwarzschild metric [69]. By introducing a different mass parameter into the metric of the Schwarzschild BH, the well-studied Damour-Solodukhin wormhole is obtained, while a procedure on the same vein on the Hayward regular BH resulted in the generalized Hayward metric as shown in eq.(1). Following [58], we re-write eq.(1) as,

$$ds^2 = -\left(1 - \frac{2\sigma x^2}{x^3 + 2\sigma\kappa^2}\right) dt^2 + \frac{dr^2}{\left(1 - \frac{2x^2}{x^3 + 2\kappa^2}\right)} + r^2(d\theta^2 + \sin^2\theta d\phi^2), \quad (3)$$

where the parameters M, M_1, ℓ are written in a dimensionless form using $\sigma = \frac{M_1}{M}$, $\kappa = \frac{\ell}{M}$ with the radial coordinate $x = \frac{r}{M}$. We will use the metric of the form given in eq.(3) for rest of the discussions. For different values of (σ, κ) , the spacetimes are classified into wormholes/BHs depending on the presence of throat/event horizon.

Fig.(1) shows the six different classes of spacetimes corresponding to different values of (σ, κ) whose properties are summarized in Table I.

	Spacetime	σ	κ	Singularity
Case I	Schwarzschild BH	1	0	✓
Case II	Schwarzschild Wormhole	0	0	✗
Case III	Damour-Solodukhin Wormhole	(0,1)	0	✗
Case IV	Hayward Wormhole	0	$(0, \frac{4}{3\sqrt{3}}]$	✗
Case V	Hayward BH	1	$(0, \frac{4}{3\sqrt{3}}]$	✗
Case VI	Hayward-Damour-Solodukhin Wormhole	(0,1)	$(0, \frac{4}{3\sqrt{3}}]$	✗

TABLE I. Table shows the classification of spacetimes into BHs and wormholes depending on the values of (σ, κ) . The only spacetime with singularity is the Schwarzschild BH while all others are regular.

III. NULL GEODESICS AND SHADOW

This section mainly reproduces the known results and sets the conventions to be used in the later sections. In this section, we revisit the derivation of critical expressions for the shadow calculations. We will be broadly following the Hamilton-Jacobi approach to calculating the null geodesics. We restrict this analysis to the static spherically symmetric solutions with the ansatz being:

$$ds^2 = -f_1(r)dt^2 + \frac{dr^2}{f(r)} + r^2 d\Omega^2, \quad (4)$$

the choice of which is motivated by the form of the generalized Hayward metric, given in eq.(3), which is the focus of this work. The effective Lagrangian for the geodesic equations in the above spacetime is given by

$$\mathcal{L} = -f_1(r)\dot{t}^2 + \frac{\dot{r}^2}{f(r)} + r^2\dot{\theta}^2 + r^2 \sin^2\theta \dot{\phi}^2,$$

whose canonical momentum is defined as

$$p_\alpha = \frac{1}{2} \frac{\partial \mathcal{L}}{\partial \dot{x}^\alpha}, \quad (5)$$

with the dot denoting derivative with respect to the affine parameter. For the static spherically symmetric metric considered, the conserved momenta (p_ϕ, p_t) , corresponding to the two Killing vectors, gives $r^2 \sin^2\theta \dot{\phi} \equiv L$ and $-f_1(r)\dot{t} \equiv -E$, respectively. The total angular momentum per unit mass and total energy per unit mass is denoted by L and E , respectively.

The Hamilton-Jacobi action given by,

$$\mathcal{S} = \frac{1}{2}\tilde{\mu}^2\lambda - Et + L\phi + S_r(r) + S_\theta(\theta),$$

which gives rise to the equation of motion the photons follow:

$$0 = \frac{E^2}{f_1(r)} - f(r) \left(\frac{\partial \mathcal{S}_r}{\partial r} \right)^2 - \frac{1}{r^2} \left(\frac{\partial \mathcal{S}_\theta}{\partial \theta} \right)^2 - \frac{1}{r^2 \sin^2 \theta} L^2. \quad (6)$$

The above equation can be decoupled into radial and angular parts as follows

$$p_\theta^2 \equiv \left(\frac{\partial \mathcal{S}}{\partial \theta} \right)^2 = \mathcal{K} - L^2 \csc^2 \theta, \quad (7)$$

$$p_r^2 \equiv \left(\frac{\partial \mathcal{S}}{\partial r} \right)^2 = \frac{1}{f(r)} \left(\frac{E^2}{f_1(r)} - \frac{\mathcal{K}}{r^2} \right), \quad (8)$$

with \mathcal{K} being the Carter constant. Without loss of generality, we can restrict our analysis to the equatorial plane ($\theta = \frac{\pi}{2}$) due to the spherical symmetry of the spacetime. This would entail $\frac{\partial \theta}{\partial \lambda} = 0$ and hence one gets $\mathcal{K} = L^2$ in such cases of equatorial motion, as is evident from eq.(7). The radial equation simplifies to

$$\frac{1}{f(r)} \dot{r} = \sqrt{\frac{1}{f(r)f_1(r)} \left(E^2 - \frac{f_1(r)\mathcal{K}}{r^2} \right)} \implies \dot{r} = L \sqrt{\frac{f(r)}{f_1(r)} \left(\frac{1}{b^2} - \frac{f_1(r)}{r^2} \right)}, \quad (9)$$

with $b = \frac{L}{E}$ being the impact parameter. The geodesic equation of motion $r(\phi)$ is thus given by

$$\left(\frac{p_r}{p_\phi} \right)^2 = \left(\frac{dr}{d\phi} \right)^2 = r^4 \frac{f(r)}{f_1(r)} \left(\frac{1}{b^2} - V_{\text{eff}} \right), \quad (10)$$

with the effective potential being of the form

$$V_{\text{eff}}(r) = \frac{f_1(r)}{r^2}. \quad (11)$$

For circular geodesics, it is known that $\dot{r} = \ddot{r} = 0$. Choosing $M = 1$ makes the coordinate x , introduced in eq.(3), equivalent to radial coordinate r . However, to avoid confusion we will use x in the following sections when discussing equations specific to the generalised Hayward metric. Hence, from eq.(8) and its derivative, we get the following set of equations,

$$\dot{x} = \frac{f(x)}{f_1(x)} \left(\frac{1}{b^2} - \frac{f_1(x)}{x^2} \right) = 0, \quad (12)$$

$$\ddot{x} = \frac{(f_1(x)f'(x) - f(r)f_1'(x))}{f_1^2(x)} \left(\frac{1}{b^2} - \frac{f_1(x)}{x^2} \right) + \frac{f(x)}{x^2 f_1(x)} \left(-f_1'(x) + \frac{2f_1(x)}{x} \right) = 0, \quad (13)$$

solving which enables us to determine the photon sphere radius x_{ph} and the corresponding impact parameter b . The critical orbits are unstable if $\ddot{r} > 0$ and stable if $\ddot{r} < 0$. Note that the unstable null circular orbits are the photon spheres and the stable null circular orbits are known as anti-photon spheres. The shadow cast by these circular null geodesics as observed by an observer located at x_o is given as

$$x_{sh}^2 = \frac{b^2}{\frac{f(x_o)}{f_1(x_o)} \left(1 - \frac{f_1(x_o)}{x_o^2} b^2\right)}. \quad (14)$$

For an observer at asymptotic infinity, due to the asymptotic flat nature of the spacetime i.e $x_o \rightarrow \infty$, the shadow radius reduces to $x_{sh} = b$.

A. Shadows with plasma medium

In reality, astrophysical objects are surrounded by an interstellar medium, generally considered to be plasma in the near horizon region. When photons pass through this plasma, they interact with it, altering the trajectory of the photons. Consequently, this interaction affects the size of the shadow of the central object as observed by a distant observer. Our current analysis focuses on homogeneous and non-homogeneous plasma profiles and observing their effect on the shadows. In this section, we will briefly discuss the impact of the plasma medium on the shadow radius following [60]. These findings will be used to analyze the effects of the above mentioned plasma profiles on generalized Hayward spacetimes.

We would restrict our analysis to the non-magnetized cold plasma with the plasma frequency of the form,

$$\omega_p(r) = \frac{4\pi e^2}{m} N(r), \quad (15)$$

where e is electron charge, m the electron mass and $N(r)$ is the number density of the electrons. The plasma medium acts as an effective refractive index for the photons propagating in this medium, and the effective refractive index is dependent on the radial coordinate r , as well as on the frequency of the photon ω , and is given by

$$n^2(r) = 1 - \frac{\omega_p^2(r)}{\omega^2}. \quad (16)$$

In presence of surrounding plasma, the null geodesic equation of motion, given in eq.(6), gets modified to

$$0 = \frac{E^2}{f_1(r)} - f(r) \left(\frac{\partial \mathcal{S}_r}{\partial r}\right)^2 - \frac{1}{r^2} \left(\frac{\partial \mathcal{S}_\theta}{\partial \theta}\right)^2 - \frac{1}{r^2 \sin^2 \theta} L^2 - \omega_p^2(r).$$

Since the plasma medium does not depend on the angular coordinates, the same technique of variable separation, as done for the vacuum case, works for this case also leads to

$$p_\theta^2 \equiv \left(\frac{\partial \mathcal{S}}{\partial \theta} \right)^2 = \mathcal{K} - L^2 \csc^2 \theta \quad (17)$$

$$p_r^2 \equiv \left(\frac{\partial \mathcal{S}}{\partial r} \right)^2 = \frac{1}{f(r)} \left(\frac{E^2}{f_1(r)} - \frac{\mathcal{K}}{r^2} - \omega_p^2(r) \right). \quad (18)$$

We get $\mathcal{K} = L^2$ by restricting the analysis to equatorial plane, since spherical symmetry still holds, similar to the vacuum case. Assuming that the frequency of photon observed by the asymptotic observer as $\omega_0 \equiv E$, for the case of asymptotically flat spacetime, the frequency ω observed by a static observer as a function of r is given by

$$\omega(r) = \frac{\omega_0}{\sqrt{f_1(r)}}, \quad (19)$$

using which the refractive index, in presence of plasma, can be written as

$$n^2 = 1 - \frac{\omega_p^2}{\frac{\omega_0^2}{f_1(r)}}. \quad (20)$$

In order to reach the asymptotic observer, the photons must satisfy $n^2 > 0$ which implies $\frac{\omega_0^2}{f_1(r)} > \omega_p^2(r)$.

Similar to the vacuum case, we translate to x coordinate and also introduce an new parameter $\Omega(x) = \frac{\omega_p^2}{E^2}$. Hence, the equivalent condition to eq.(12) and (13) for the circular orbits in presence of plasma is,

$$\dot{x} = \frac{f(x)}{f_1(x)} \left(\frac{1}{b^2} - \frac{f_1(x)}{x^2} - \frac{\Omega(x)f_1(x)}{b^2} \right) = 0 \quad (21)$$

$$\ddot{x} = \left(\frac{f(x)}{f_1(x)} \right)' \left(\frac{1}{b^2} - \frac{f_1(x)}{x^2} - \frac{\Omega(x)f_1(x)}{b^2} \right) + \frac{f(x)}{f_1(x)} \left(-\frac{f_1'(x)}{x^2} + \frac{2f_1(x)}{x^3} - \frac{(\Omega(x)f_1(x))'}{b^2} \right) = 0 \quad (22)$$

Using the above equations, the impact parameter can be written in terms of the photon sphere radius x_{ph} as,

$$b^2 = \frac{x^2}{f_1} (1 - \Omega f_1) \Big|_{x=x_{\text{ph}}}. \quad (23)$$

The x_{ph} has two possible branches of solutions given by

$$f(x) = 0, \quad (24)$$

$$\frac{1}{f_1(x)} (1 - \Omega(x)f_1(x)) \left(-f_1'(x) + \frac{2f_1(x)}{x} \right) - (\Omega(x)f_1(x))' = 0. \quad (25)$$

The shadow radius observed by an observer at x_o is given by

$$x_{\text{sh}}^2 = \frac{\frac{x_{\text{ph}}^2}{f_1(x_{\text{ph}})} (1 - \Omega(x_{\text{ph}})f_1(x_{\text{ph}}))}{\frac{f(x_o)}{f_1(x_o)} \left(1 - \frac{b^2}{x_o^2} f_1(x_o) - \Omega(x_o)f_1(x_o)\right)}. \quad (26)$$

For an asymptotic observer at $x_o \rightarrow \infty$, the shadow radius simplifies to

$$x_{\text{sh}}^2 \Big|_{x_o \rightarrow \infty} = \frac{\frac{x_{\text{ph}}^2}{f_1(x_{\text{ph}})} (1 - \Omega(x_{\text{ph}})f_1(x_{\text{ph}}))}{(1 - \Omega(\infty))}. \quad (27)$$

Note that the numerator in the above equation is required to be positive as it represents the impact parameter, as shown in eq.(23), which is a physical quantity and hence cannot be negative.

Now let us apply the above results to the two plasma profiles we are interested. We begin by considering the homogeneous plasma profile given by $\Omega = k_0$. Solving equations (24) and (25) with $\Omega = k_0$ gives the impact parameter

$$b^2 = \frac{x_{\text{ph}}^2}{f_1(x_{\text{ph}})} (1 - k_0 f_1(x_{\text{ph}})) \quad (28)$$

with the shadow radius obtained from eq.(27)

$$x_{\text{sh}}^2 = \frac{\frac{x_{\text{ph}}^2}{f_1(x_{\text{ph}})} (1 - k_0 f_1(x_{\text{ph}}))}{(1 - k_0)}. \quad (29)$$

Since the impact parameter, given by eq.(28), is a physical quantity which needs to be positive, the denominator of eq.(29) also needs to be positive, hence giving $0 \leq \kappa_0 < 1$. Further constraints on this parameter would depend on the refractive index condition and will be studied for each spacetime from the generalised Hayward metric.

For the non-homogeneous case, $\Omega = \frac{k_x}{x}$. Similar to the homogeneous profile, solving equations (24) and (25) we get the impact parameter to be

$$b^2 = \frac{x_{\text{ph}}^2}{f_1(x_{\text{ph}})} \left(1 - \frac{k_x}{x_{\text{ph}}} f_1(x_{\text{ph}})\right). \quad (30)$$

Note that as $x \rightarrow \infty$, the plasma profile $\Omega \rightarrow 0$, hence the shadow radius in eq.(27) reduces to

$$x_{\text{sh}}^2 = b^2 = \frac{x_{\text{ph}}^2}{f_1(x_{\text{ph}})} \left(1 - \frac{k_x}{x_{\text{ph}}} f_1(x_{\text{ph}})\right). \quad (31)$$

In this case, the constraints on the plasma profile parameter are obtained from the impact parameter and the refractive index, which need to be analyzed for each spacetime. No broad statements can be made at this point for the general function.

IV. SHADOW OF GENERALISED HAYWARD METRIC

In this section, we will apply the above results for the various spacetimes of the generalized Hayward metric given in eq.(3). and summarized in Table I.

A. Schwarzschild black hole $\sigma = 1, \kappa = 0$:

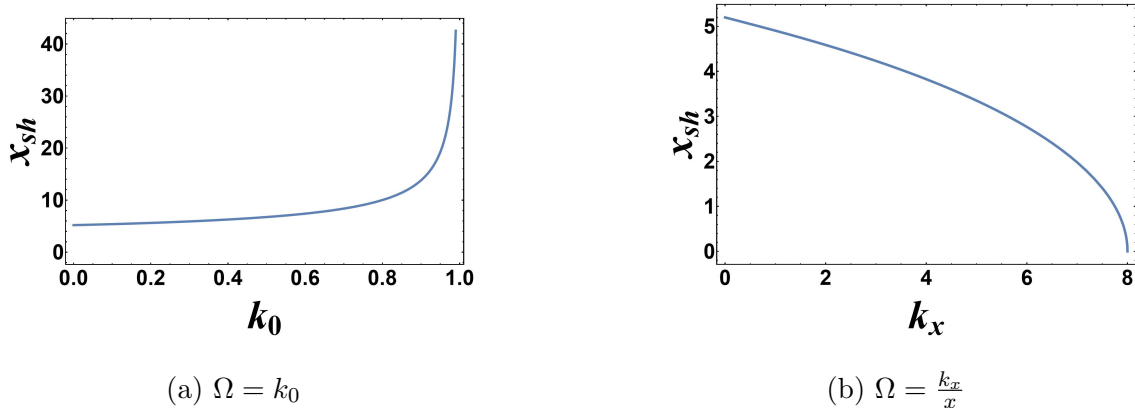


FIG. 2. Plots showing variation of the shadow radius of the Schwarzschild BH as a function of the plasma parameter. The left and right panels denote the effect of the homogeneous and non-homogeneous plasma profiles on the shadow radius, respectively.

By setting $\sigma = 1, \kappa = 0$ in eq.(3), we recover the standard Schwarzschild solution. The shadow radius of Schwarzschild BH was first analyzed by [36]. This is one of the most well-known results in the literature, and we include these results for completeness. Solving eqns.(12) and (13), we get $x_{\text{ph}} = 3, b^2 = 27$ and the shadow radius being $x_{\text{sh}} = 3\sqrt{3}$.

We now focus on the influence of the plasma on the shadow of Schwarzschild BH. For the case of homogeneous plasma, the eq.(24) does not lead to any solutions. However, eq.(25) reduces to

$$(1 - k_0)x^2 + (4k_0 - 3)x - 4k_0 = 0. \quad (32)$$

Solving this quadratic equation we find that the $x_{\text{ph}} > x_{\text{h}}$ for all the range of k_0 where x_{h} is the horizon radius. Note that the shadow radius diverges at $k_0 \rightarrow 1$, which is observed in the Fig.2a.

Similarly, for the case of non-homogeneous plasma, the eq.(25) reduces to

$$2x^3 + (-k_x - 6)x^2 + 4k_x x - 4k_x = 0. \quad (33)$$

Substituting the solution of the above equation in eq.(31), it can be checked that the shadow radius becomes zero at $k_x = 8$, beyond which the photon sphere does not exist. The shadow radius decreases monotonically as a function of the plasma parameter k_x as shown in Fig.2b.

B. Schwarzschild Wormhole $\sigma = 0, \kappa = 0$:

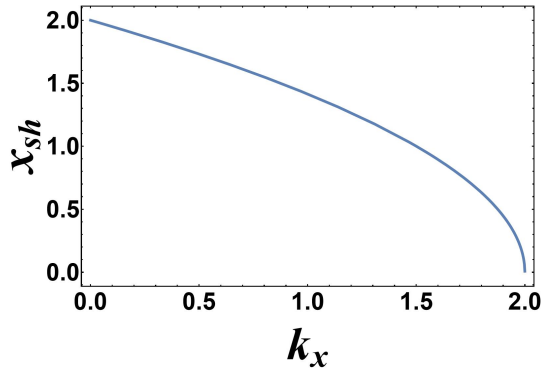


FIG. 3. Plot shows the monotonic decrease of the shadow radius for the Schwarzschild Wormhole with increasing non-homogeneous plasma parameter where the plasma profile is given as $\Omega = \frac{k_x}{x}$. Physical solutions exist till $k_x = 2$.

For $\sigma = \kappa = 0$, the metric functions in eq.(3) become $f_1(x) = 1$ and $f(x) = 1 - \frac{2}{x}$. Solving eq.(12),(13) we get $x_{\text{ph}} = 2$, $b^2 = x_{\text{ph}}^2 = 2$, $x_{\text{sh}} = \sqrt{b^2} = 2$.

Now we look at the influence of plasma on the shadow of Schwarzschild wormhole spacetime. For the case of homogeneous plasma profile, we observe that the photon sphere is still located at the throat $x = 2$ obtained from solving $f(x) = 0$. Since $f_1(x) = 1$, the shadow radius from eq.(29) becomes independent of the plasma parameter k_0 . Hence it is identical to the vacuum case.

Moving on to the case of non-homogeneous plasma profile, the photon sphere equations (24) and (25) provide us with the solutions $x_{\text{ph}} = 2$ and $x_{\text{ph}} = 2 - k_x$. The shadow radius corresponding to the two photon radius is thus $x_{\text{sh}}^2 = 2(2 - k_x)$ and $x_{\text{sh}}^2 = -\frac{k_x}{4}$ respectively. Of the above solutions, only the first one is physically reasonable. Hence, from $x_{\text{sh}}^2 = 2(2 - k_x)$, we can deduce that the shadow radius decreases monotonically with increasing plasma parameter k_x . At $k_x = 2$, the shadow radius vanishes and becomes unphysical beyond this point as shown in Fig.3.

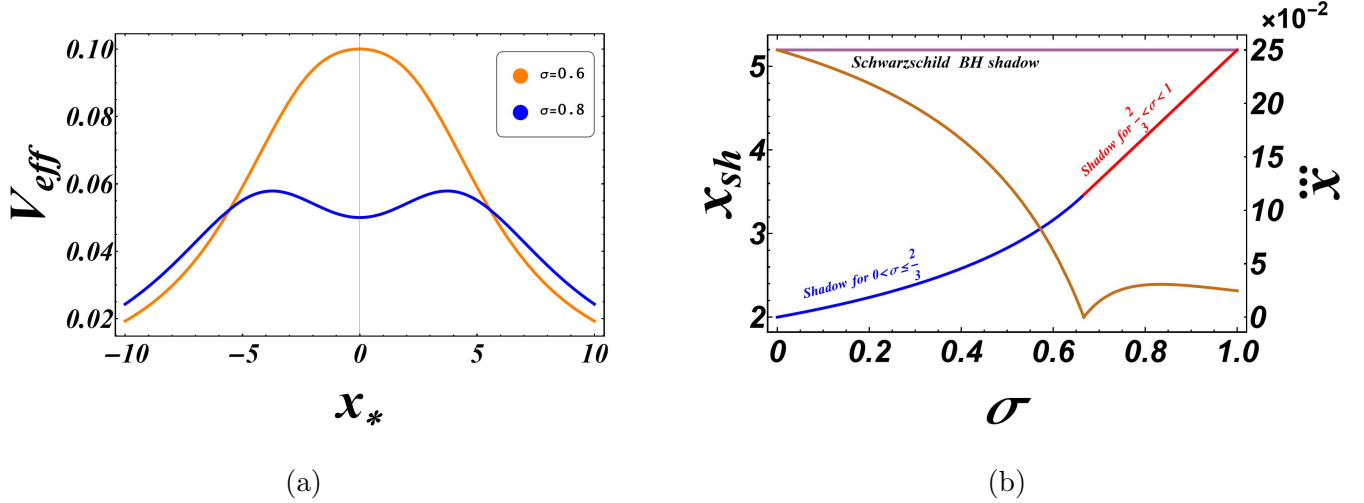


FIG. 4. (a) The plot shows the variation of the effective potential for the Damour-Solodukhin wormhole as a function of tortoise coordinate x_* . The nature of the effective potential depends on the parameter σ . (b) The plot shows the shadow radius for the complete range of the parameter σ which are compared with the Schwarzschild BH shadow denoted by the violet line. The brown line shows the variation of \ddot{x} which is positive for the complete range indicating that the photon spheres are unstable.

C. Damour-Solodukhin Wormhole $0 < \sigma < 1, \kappa = 0$:

For the Damour-Solodukhin wormhole, the metric components simplify to $f_1(x) = 1 - \frac{2\sigma}{x}$ and $f(x) = 1 - \frac{2}{x}$. Unlike the previous cases, for this wormhole we have two possible solutions to eq.(12), which will be discussed in detail one by one. The first set of solutions corresponds to $f(x) = 0$, which gives $x_{ph} = 2$. The critical impact parameter for this is obtained by solving eq.(13), which gives $b^2 = \frac{4}{1-\sigma}$. It is evident that these circular geodesics are located at the throat. Note that the photons will be observable to an asymptotic observer only if the photon orbits are unstable which is determined by the condition $\ddot{x}|_{x=x_{ph}} > 0$. Hence we check the stability of the null geodesics by computing $\ddot{x}|_{x=x_{ph}}$ which for this first set of solutions is given by

$$\ddot{x}|_{x=x_{ph}} = \frac{2 - 3\sigma}{8(1 - \sigma)}. \quad (34)$$

From the above expression we obtain the following condition on σ ,

$$\ddot{x}|_{x=x_{\text{ph}}} > 0 \quad \Longrightarrow \quad 0 < \sigma < \frac{2}{3} \quad \Longrightarrow \quad \text{photon sphere} \quad (35)$$

$$\ddot{x}|_{x=x_{\text{ph}}} < 0 \quad \Longrightarrow \quad \frac{2}{3} < \sigma < 1 \quad \Longrightarrow \quad \text{anti-photon sphere} \quad (36)$$

The shadow radius for the range of parameter $0 < \sigma < \frac{2}{3}$ is thus obtained from this set of solution i.e. $x_{\text{ph}} = 2$ and $b^2 = \frac{4}{1-\sigma}$ as shown by the blue curve in Fig.(4b). For $\sigma = \frac{2}{3}$, the \ddot{x} is identically 0 and higher order derivative tests are performed to ensure that the unstable photon sphere exists at $x = 2$. The second set of solutions to eq.(12), along with eq.(13),

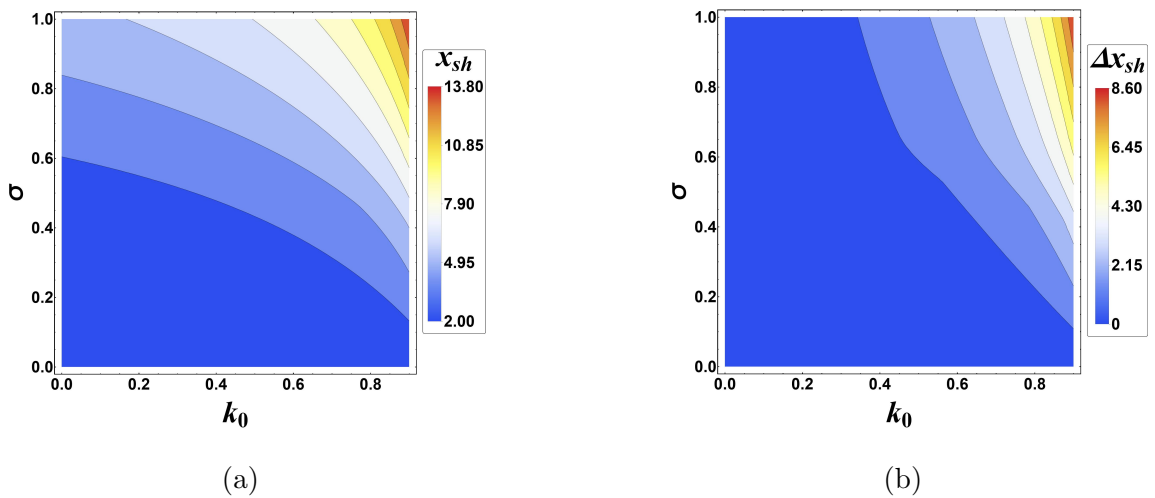


FIG. 5. Figure shows the effect of homogeneous plasma profile given by $\Omega = k_0$ on the shadow radius of the Damour-Solodukhin wormhole. (a) The plot shows the variation of the shadow radius as a function of σ and k_0 . Larger shadow radius is observed for higher values of both σ and k_0 . (b) The plot shows the variation of the difference $\Delta x_{\text{sh}} = x_{\text{sh}} - x_{\text{sh}}|_{k_0=0}$ between the shadow radius with and without plasma, as a function of σ and k_0 .

gives $x_{\text{ph}} = 3\sigma$ and $b^2 = 27\sigma^2$. This set of solutions are only valid when $\sigma \geq \frac{2}{3}$ since below this value, the photon sphere radius would be located inside the throat radius and thus will not be part of the manifold. The stability condition for this case reduces to

$$\ddot{x}|_{x=x_{\text{ph}}} = \frac{2(3\sigma - 2)}{81\sigma^5}, \quad (37)$$

which implies

$$\ddot{x}|_{x=x_{\text{ph}}} > 0 \quad \Longrightarrow \quad \frac{2}{3} < \sigma < 1 \quad \Longrightarrow \quad \text{photon sphere.} \quad (38)$$

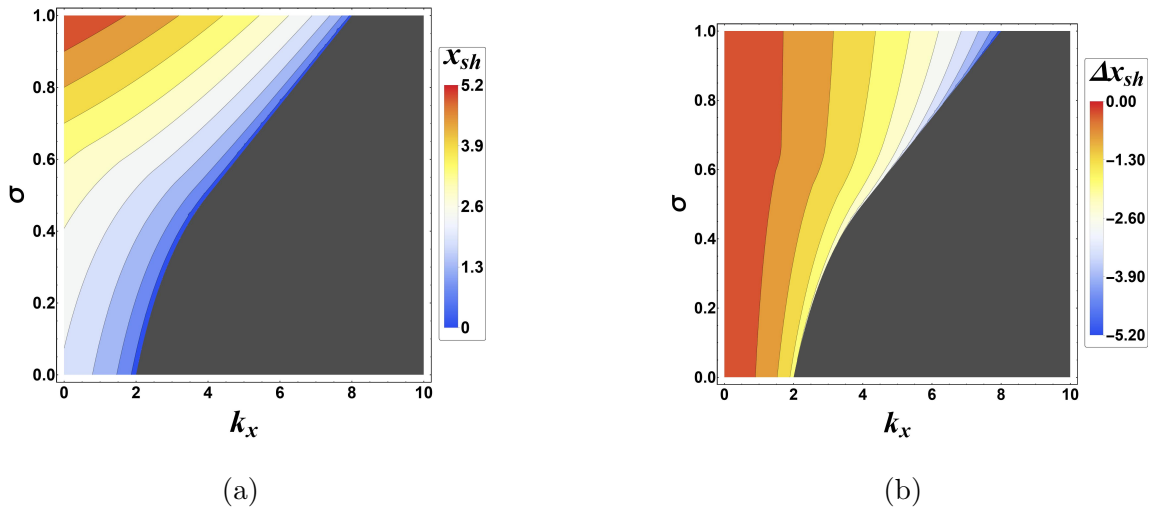


FIG. 6. Figure shows the effect of non-homogeneous plasma profile given by $\Omega = \frac{k_x}{x}$ on the shadow radius of the Damour-Solodukhin wormhole. The grey region represents the values of parameters for which there is no shadow. (a) The plot shows the variation of the shadow radius as a function of σ and k_x . Larger shadow radius is observed for higher values of σ and smaller values of k_x , unlike the homogeneous plasma case. (b) The plot shows the variation of the difference $\Delta x_{\text{sh}} = x_{\text{sh}} - x_{\text{sh}}|_{k_x=0}$ between the shadow radius with and without plasma, as a function of σ and k_x .

Thus the shadow radius for parameter range $\frac{2}{3} < \sigma < 1$ is obtained using $x_{\text{ph}} = 3\sigma$ and $b^2 = 27\sigma^2$ as shown by the red curve in Fig.(4b). As $\sigma \rightarrow 0$, the shadow of the wormhole approaches that of the Schwarzschild BH denoted by the violet line in Fig.(4b) for comparison. The \ddot{x} is positive for all values of x_{sh} and σ denoted by the brown curve in Fig.(4b) which indicates their instability.

The difference in the two branches of the solutions of eq.(12), as mentioned above, can be clearly seen from the effective potential plots shown in Fig.4a, where the nature of the potential changes from a single to a double peak with the critical point being $\sigma = \frac{2}{3}$. The potential for the wormhole is plotted as a function of tortoise coordinate x_* which is defined as $dx_*^2 = \frac{dx^2}{f_1(x)f(x)}$ and ranges from $(-\infty, \infty)$.

We now move on to study the effect of plasma on the shadow of this wormhole. For the homogeneous plasma profile, the variation of the shadow radius as a function of σ and plasma parameter k_0 is shown in Fig.5a. Large values of x_{sh} is seen for higher values of both σ and k_0 . To highlight the effect of plasma, we also plot the difference in shadow radius

between the with and without plasma cases denoted by $\Delta x_{\text{sh}} = x_{\text{sh}} - x_{\text{sh}}|_{k_0=0}$ as shown in Fig.5b. For the case of non-homogeneous plasma, the x_{sh} and Δx_{sh} are shown in Fig.6a and Fig.6b, respectively. Unlike the homogeneous case, we observe that the shadow radius reduces as the plasma parameter k_x increases.

D. Hayward Wormhole: $\sigma = 0$, $0 < \kappa \leq \frac{4}{3\sqrt{3}}$

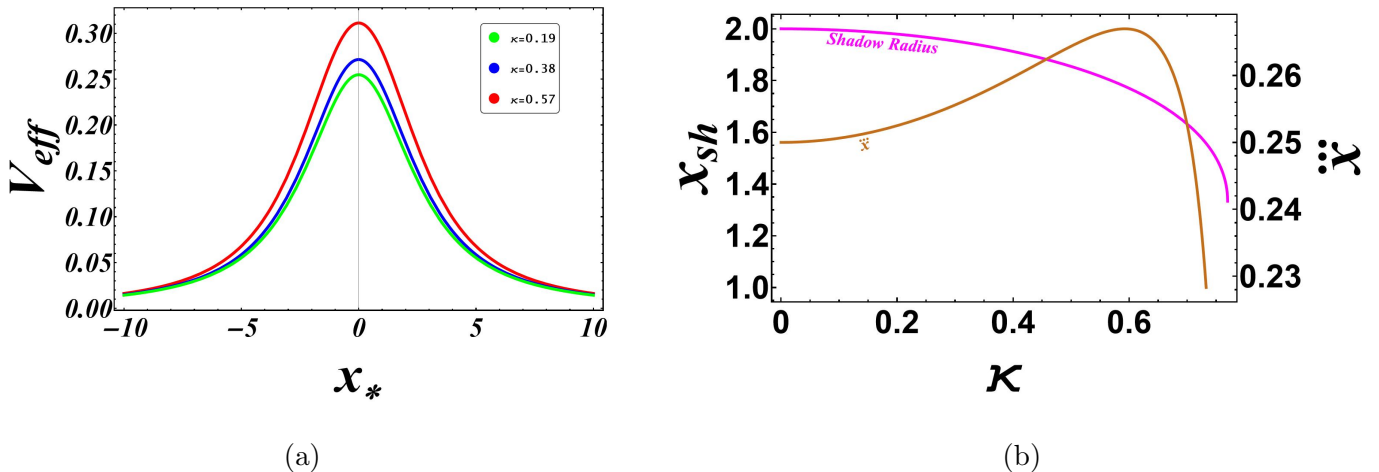


FIG. 7. (a) The plot shows the single peak effective potential for a few representative values of κ for the Hayward wormhole. This feature holds for the entire parameter range of κ . (b) The plot shows the variation of the shadow radius (magenta curve) as a function of κ while the brown curve indicates the stability of the photon spheres denoted by \ddot{x} , the positive value of which, for the entire parameter range, indicates the photon spheres to be unstable.

The metric functions are of the form $f_1(x) = 1$ and $f(x) = 1 - \frac{2x^2}{x^3 + 2\kappa^2}$ for the Hayward wormhole spacetime. The only possible solution to eq.(12) and eq.(13), for this wormhole, is $f(x) = 0$ and $b^2 = x_{\text{ph}}^2$. Hence for this case, the circular photon orbits are located at the throat, which is defined as the largest root to the cubic polynomial equation $f(x) = 0$ i.e. $x^3 + 2\kappa^2 - 2x^2 = 0$. We plot the effective potential as a function of the tortoise coordinates shown in Fig.7a, which is characterized by a single peak for all values of κ . To understand the stability of photon orbits, we compute \ddot{x} numerically and conclude that these orbits are unstable for the complete range of κ as shown by the brown curve in Fig.(7b). The instability of the photon spheres is evident from the effective potentials as well since for the complete

range of κ have a single peak around the throat. Finally, we observe that the shadow radius reduces monotonically with increasing κ as shown by the magenta curve in Fig7b. For

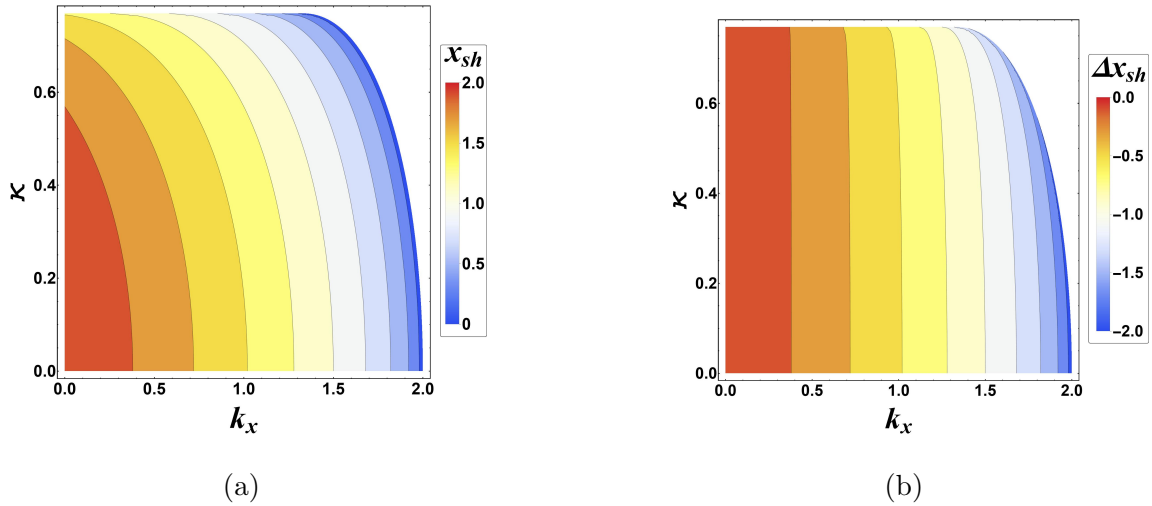


FIG. 8. The plots show the effect of the non-homogeneous plasma profile given by $\Omega = \frac{k_x}{x}$, on the shadow of the Hayward wormhole. (a) The variation of x_{sh} is shown as a function of κ and k_x which reduces as k_x increases for a particular κ . (b) The difference in shadow radius $\Delta x_{\text{sh}} = x_{\text{sh}} - x_{\text{sh}}|_{k_x=0}$, with and without plasma, is shown as function of κ and k_x .

the case of homogeneous plasma, it can be checked from eq.(29) that the shadow radius is independent of the plasma parameter and is identical to the vacuum case. However, for the case of non-homogeneous plasma, the shadow radius decreases as the plasma parameter k_x increases as shown in Fig.8a. We also show the variation of $\Delta x_{\text{sh}} = x_{\text{sh}} - x_{\text{sh}}|_{k_x=0}$ in Fig.8b with varying κ and k_x that highlights the deviation of shadow radius from the vacuum case in presence of non-homogeneous plasma.

E. Regular Hayward black hole: $\sigma = 1$, $0 < \kappa \leq \frac{4}{3\sqrt{3}}$

Setting $\sigma = 1$, $0 < \kappa \leq \frac{4}{3\sqrt{3}}$ reduces the metric in eq.(3) to that of the regular Hayward BH case which was the original metric to be deformed to give rise to the generalized metric. The metric functions reduce to $f_1(x) = f(x) = 1 - \frac{2x^2}{x^3 + 2\kappa^2}$ and is characterized with two horizons corresponding to the roots of $g_{tt} = 0$. Solving eq.(12) for the photon sphere radius results in a sixth-order polynomial equation, which has been solved numerically. The polynomial equation has only two positive roots ($x_{\text{ph1}}, x_{\text{ph2}}$), of which, we are interested in

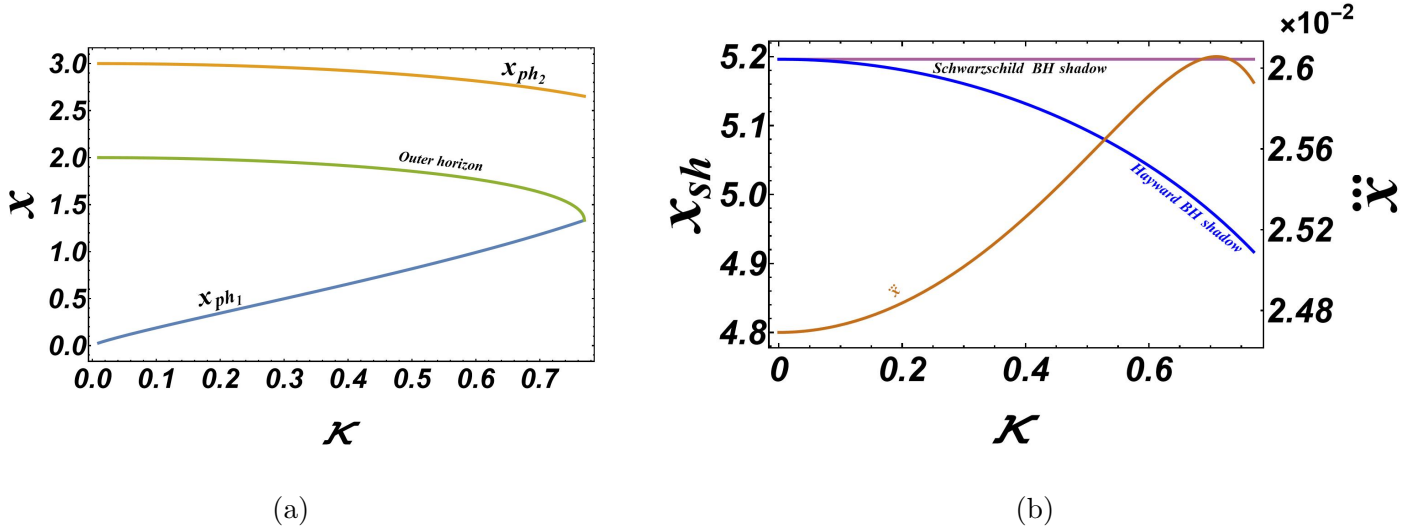


FIG. 9. (a) The plot shows the relative location of the two positive photon spheres with respect to the outer horizon. Only the larger of the two photon spheres lies outside the horizon and, hence, the only physically relevant solution for generating shadow. (b) The plot shows the shadow radius of the Hayward BH in blue along with the Schwarzschild BH shadow radius in violet for comparison. The brown curve represents \ddot{x} , which is positive for the complete range of parameters, indicating that the photon sphere is indeed unstable.

the one outside the outer horizon. Fig.9a shows the position of (x_{ph1}, x_{ph2}) with respect to the outer horizon. The larger of the two photon spheres, i.e. x_{ph2} , denoted by the brown curve in Fig.9a, lies outside the outer horizon and hence gives rise to the shadow. We then calculate the \ddot{x} for the photon orbit corresponding to x_{ph2} shown in brown curve in Fig.9b and conclude that they are all unstable. The corresponding shadow radius is shown as the blue curve in Fig.9b where the Schwarzschild shadow radius (magenta curve) is also shown for comparison.

The introduction of homogeneous plasma profile leads to increase in shadow radius with increasing k_0 as shown in Fig.(10a) while the reduction in the shadow radius is seen for the non-homogeneous plasma as the plasma parameter k_x increases, shown in Fig.(11a). The difference in the shadow radius in the presence and absence of plasma is shown as a function of metric and plasma parameters in Fig.10b for the homogeneous plasma and in Fig.11b for the non-homogeneous case.

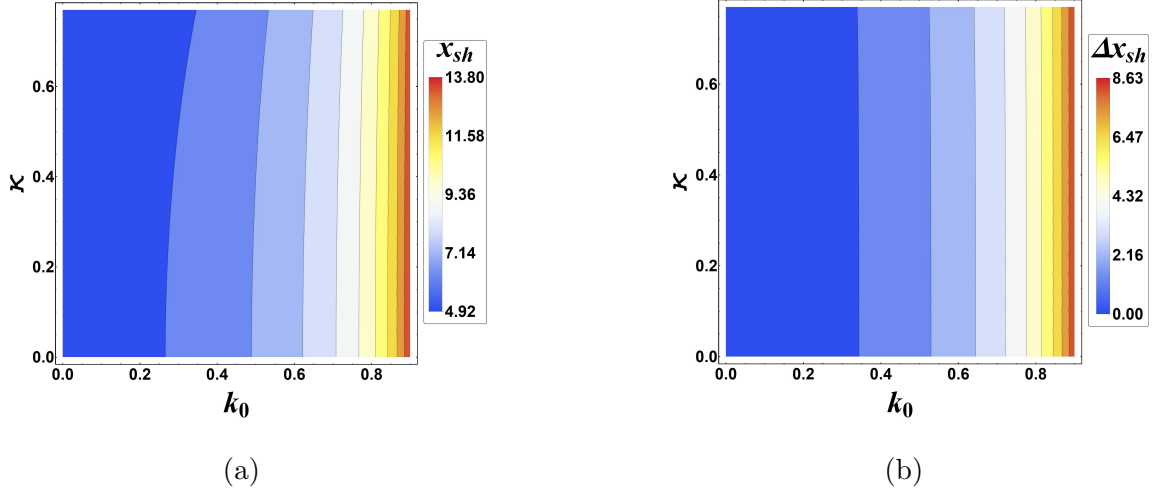


FIG. 10. The plots correspond to the shadow radius of the Hayward regular BH in presence of the homogeneous plasma profile given by $\Omega = k_0$. (a) The plot shows the variation of shadow radius as a function of κ and k_0 . (b) The plot shows the difference in shadow radius with and without plasma i.e. $\Delta x_{\text{sh}} = x_{\text{sh}} - x_{\text{sh}}|_{k_0=0}$, as a function of κ and k_0 .

F. Hayward-Damour-Solodukhin wormhole: $0 < \sigma < 1$, $0 < \kappa \leq \frac{4}{3\sqrt{3}}$

This wormhole spacetime is the most general case spanning the entire range of (σ, κ) . The metric functions for this class are given by $f_1(x) = 1 - \frac{2\sigma x^2}{x^3 + 2\sigma\kappa^2}$ and $f(x) = 1 - \frac{2x^2}{x^3 + 2\kappa^2}$. There are two branches of solutions for eq.(12) given by $f(x) = 0$ and $-f'_1(x) + \frac{2f_1(x)}{x} = 0$. These solutions determine the radius of the circular photon orbits and the impact parameter is given by eq.(13) which reduces to $b^2 = \frac{x_{\text{ph}}^2}{f_1(x_{\text{ph}})}$ for this case. These equations have been solved numerically, and we observe that in this wormhole geometry, there are either one, two, or three photon spheres depending on the value of metric parameters. We have plotted the number of photon orbits as a function of parameters in Fig.12. Note that for certain choices of parameters there are no photon spheres denoted by the black region of Fig.12. In the case of single-peak potential, the photon sphere is located near the throat, and for the double-peak potential, the photon orbits at the throat is an anti-photon sphere. For the triple peak potential, there are two photon spheres out of which one is located at the throat, and the two photon spheres are separated by an anti-photon sphere. To get a better visual representation of these scenarios, we have plotted the effective potential for specific parameters to cover all the possible cases in Fig.13a. We compute the shadow radius corresponding to the largest

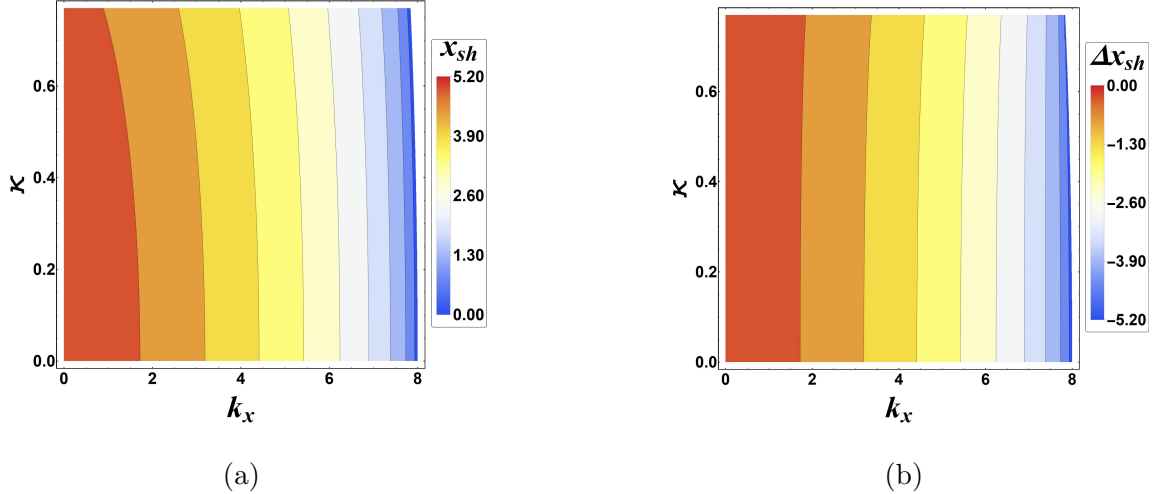


FIG. 11. The plots show the effect of non-homogeneous plasma profile given by $\Omega = \frac{k_x}{x}$ on the shadow of the regular Hayward BH. (a) The plot shows the variation in shadow radius as a function of κ and k_x . (b) The plot shows the difference in shadow radius in presence and absence of plasma, i.e. $\Delta x_{\text{sh}} = x_{\text{sh}} - x_{\text{sh}}|_{k_x=0}$, as a function of κ and k_x .

of the photon spheres in case there are more than one photon sphere. The shadow radius for the complete parameter range of σ and κ is plotted in Fig.13b. Larger shadow radius is observed for higher σ and for a particular choice of κ .

Finally, we move on to study the effect of plasma on the shadow of this wormhole metric. We plot the shadow radius and their difference with and without plasma for both homogeneous and non-homogeneous profiles in Fig.14 and 15 respectively. Since the variation of multiple parameters and their effect on shadow cannot be studied simultaneously, we choose certain representative parameter sets and study the effect of plasma on their shadows. For the homogeneous plasma profile, we observe that the shadow radius increases as the plasma parameter k_0 increases as shown in Fig.14a. However, for the case of non-homogeneous plasma, the shadow radius decreases as the plasma parameter k_x reduces as shown in Fig.15a. To complete the analysis we also plot the difference in the shadow radius with and without plasma for both homogeneous and non-homogeneous profiles as shown in Fig.14b and 15b respectively.

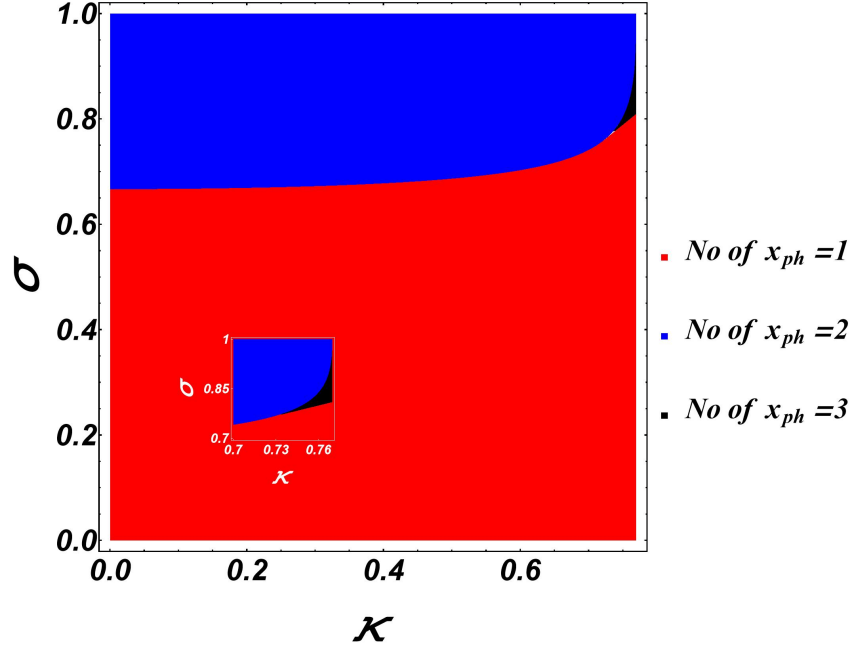


FIG. 12. The plot shows the number of photon spheres occurring for different choices of (σ, κ) in case of the Hayward-Damour-Solodukhin wormhole. In case of multiple photon spheres, only the largest one is considered to be casting the observed shadow. The points $\sigma = \kappa = 0$ and $\sigma = 1$ are not part of the spacetime and the plot starts just after these values.

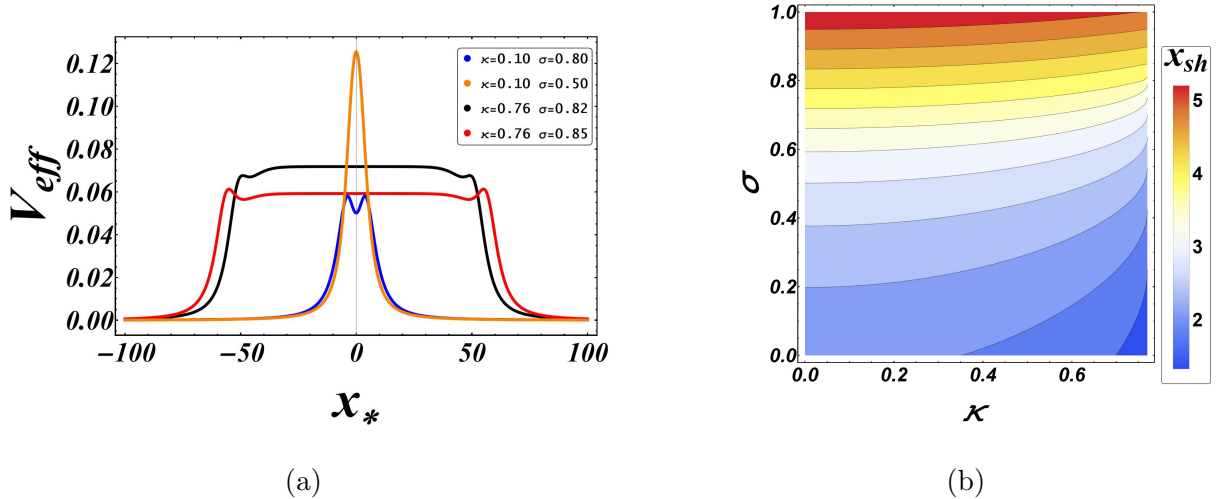


FIG. 13. (a) The plot shows the effective potentials for different choices of (σ, κ) for the Hayward-Damour-Solodukhin wormhole. The orange curve represents a single barrier, the blue curve represents a double barrier, and the red and black ones represent triple barrier potentials. (b) The plot shows the shadow radius for the complete range of metric parameters.

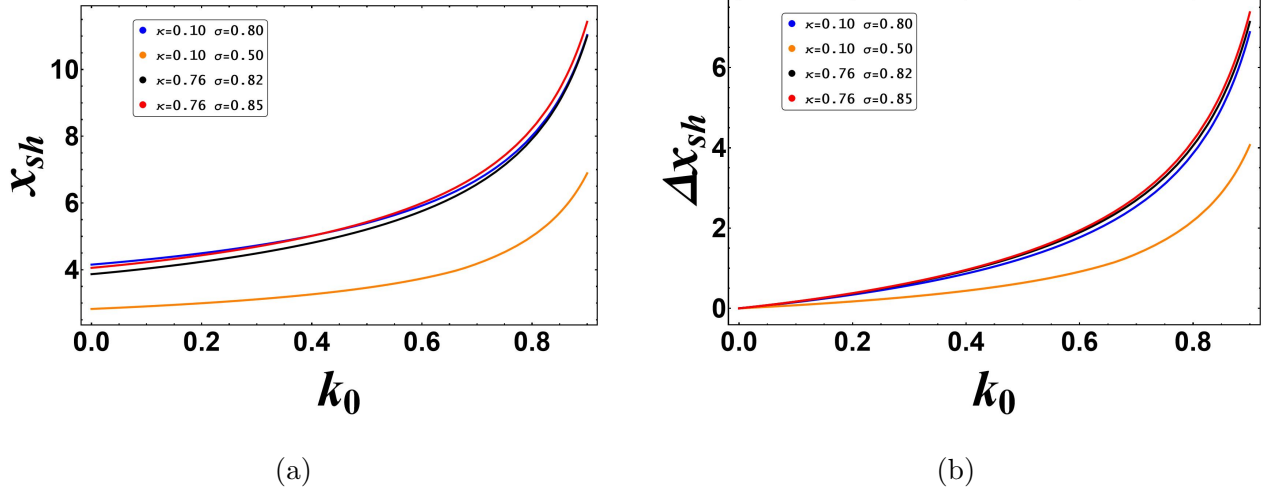


FIG. 14. (a) The plot shows the variation of shadow radius for certain representative choices of (σ, κ) in the presence of homogeneous plasma profile of the form $\Omega = k_0$ for the Hayward-Damour-Solodukhin wormhole. The effective potential for these same set of (σ, κ) has been shown in Fig.13a. (b) The plot shows the difference in shadow radius with and without plasma i.e. $\Delta x_{sh} = x_{sh} - x_{sh}|_{k_0=0}$.

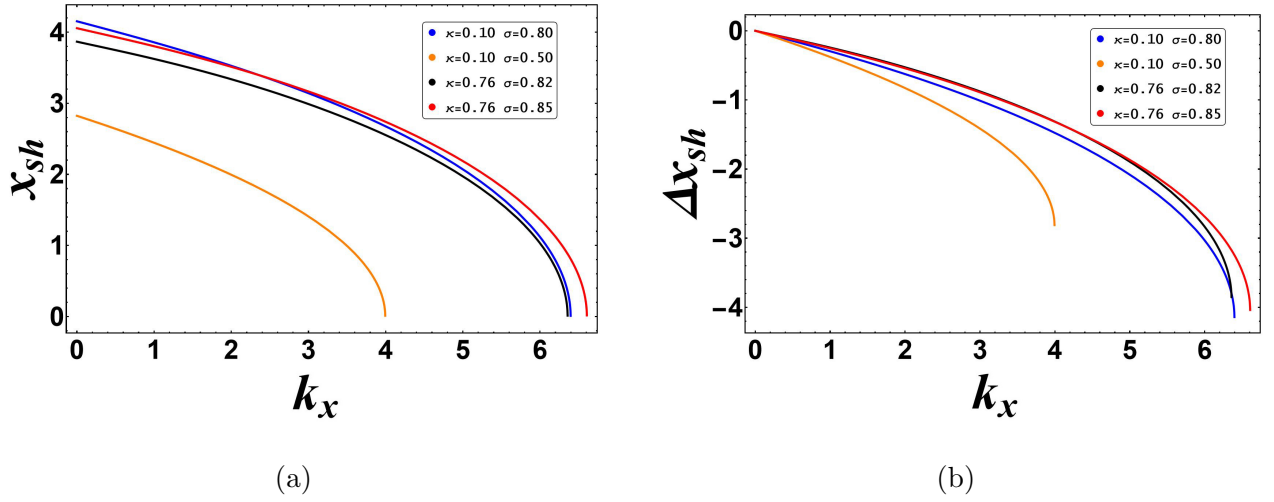


FIG. 15. The plot shows the variation of shadow radius for certain representative choices of (σ, κ) in the presence of non-homogeneous plasma profile of the form $\Omega = \frac{k_x}{x}$ for the Hayward-Damour-Solodukhin wormhole. The effective potential for these same set of (σ, κ) has been shown in Fig.13a. (b) The plot shows the difference in shadow radius with and without plasma i.e. $\Delta x_{sh} = x_{sh} - x_{sh}|_{k_x=0}$.

Spacetime	Vacuum		Homogeneous plasma	Non-homogeneous plasma
	(σ, x_{sh})	(κ, x_{sh})	(k_0, x_{sh})	(k_x, x_{sh})
Schwarzschild BH	$(1, -)$	$(0, -)$	(\uparrow, \uparrow)	(\uparrow, \downarrow)
Schwarzschild WH	$(0, -)$	$(0, -)$	$(k_0, -)$	(\uparrow, \downarrow)
DS WH	(\uparrow, \uparrow)	$(0, -)$	(\uparrow, \uparrow)	(\uparrow, \downarrow)
Hayward WH	$(0, -)$	(\uparrow, \downarrow)	$(k_0, -)$	(\uparrow, \downarrow)
Hayward BH	$(1, -)$	(\uparrow, \downarrow)	(\uparrow, \uparrow)	(\uparrow, \downarrow)
Case VI WH	(\uparrow, \uparrow)	(\uparrow, \downarrow)	(\uparrow, \uparrow)	(\uparrow, \downarrow)

TABLE II. Table shows the summary of the results obtained in our study. For each spacetime, the dependence of the shadow radius (x_{sh}) on the metric and plasma parameters is shown for vacuum and in presence of homogeneous and non-homogeneous plasma profiles. When studying the dependence of x_{sh} on a particular parameter, the other parameters are kept fixed. The (\uparrow, \downarrow) indicates increasing and decreasing values respectively. In some cases, the x_{sh} is constant and does not depend on the parameters and are denoted by ‘-’.

V. CONCLUSION

In this work, we have performed a detailed investigation of the shadows of various classes of spacetimes arising from different parameter ranges of the generalized Hayward metric [58]. The metric in eq.(3) depends on parameters (σ, κ) and is obtained from the Hayward regular BH metric by introducing different mass parameters in the g_{tt} and g_{rr} components. This metric gives rise to four distinct kinds of wormholes, a regular and a singular BH solution as shown in Fig.(1) and listed in Table I. The properties of each spacetime and their quasinormal mode frequencies have been studied in [58]. Interestingly, during the calculation of the shadow radius of these spacetimes, we observed that in the most general case, i.e. the Hayward-Damour-Solodukhin wormhole, there are two photon spheres for a specific range of (σ, κ) . The effective potential for this general class of wormhole exhibits single, double and triple peaks depending on the values of the metric parameters. The shadow radius for this wormhole increases as σ increases, keeping κ fixed while it decreases with increasing κ , with the value of σ being fixed. The remaining wormhole and BH spacetimes are characterised by only one photon sphere.

We have studied the dependence of the shadow radius on the metric parameters for all the spacetimes and also noted their deviation from the Schwarzschild BH shadow, which occurs for $(\sigma = 1, \kappa = 0)$. This analysis is essential in the context of BH mimickers where certain choices of metric parameters can result in non-singular spacetimes producing shadow radii that are indistinguishable from those of a Schwarzschild BH. We have noticed that for the Hayward regular BH, the shadow radius closely matches with that of the Schwarzschild BH for small values of κ , as shown in Fig.(9b). Similarly, for the Damour-Solodukhin wormhole, the shadow radius approaches that of the Schwarzschild BH as $\sigma \rightarrow 1$, as seen in Fig.(4b). However, the shadows of both these geometries begin to deviate from the Schwarzschild shadow as κ increases for the Hayward regular BH and as σ becomes smaller for the Damour-Solodukhin wormhole. This is expected, as in these limits of metric parameters, the differences in the metric of these geometries become more pronounced from a Schwarzschild BH.

The above conclusions are for shadows of spacetimes when considered in vacuum i.e. in absence of any surrounding medium around the compact object. However, in real astrophysical scenarios the compact objects exist in environments. To understand the effect of such

non-vacuum environment on the shadow radius, as a first step, we consider plasma surrounding the compact objects. For analytical simplicity, we focused on specific plasma profiles, namely, homogeneous ($\Omega(r) = k_0$) and non-homogeneous plasma profiles ($\Omega(r) = \frac{kx}{x}$). We calculated the effects of these plasma profiles for all the classes of spacetimes and also highlighted the difference in the shadow radius in the presence and absence of plasma. The summary of the dependence of shadow radius on the metric as well as plasma parameters for all spacetimes is given in Table II. A more realistic plasma profile cannot be handled analytically and would require a numerical approach, including other nontrivial effects such as magnetic fields and accretion, to name a few. This is well beyond this paper's scope and will be addressed in future projects. Hence, in summary, our generalised Hayward metric provides the perfect ground for studying the shadow of various regular/singular compact objects.

ACKNOWLEDGEMENTS

SG acknowledges Rajibul Shaikh for constructive discussions. PDR acknowledges the support from Infosys foundation. SC would like to acknowledge Mathematical Research Impact Centric Support (MATRICS) grant (MTR/2022/000318) from the Science and Engineering Research Board (SERB) of India.

-
- [1] J. B. Hartle, Solar system tests of general relativity, in *Gravity: An Introduction to Einstein's General Relativity* (Cambridge University Press, 2021) p. 219–233.
 - [2] B. P. Abbott *et al.* (LIGO Scientific, Virgo), *Phys. Rev. Lett.* **116**, 061102 (2016), arXiv:1602.03837 [gr-qc].
 - [3] K. Akiyama *et al.* (Event Horizon Telescope), *Astrophys. J. Lett.* **875**, L1 (2019), arXiv:1906.11238 [astro-ph.GA].
 - [4] M. S. Morris, K. S. Thorne, and U. Yurtsever, *Phys. Rev. Lett.* **61**, 1446 (1988).
 - [5] M. S. Morris and K. S. Thorne, *American Journal of Physics* **56**, 395 (1988), <https://doi.org/10.1119/1.15620>.
 - [6] A. Ori, *Phys. Rev. Lett.* **67**, 789 (1991).

- [7] E. Poisson and W. Israel, *Phys. Rev. Lett.* **63**, 1663 (1989).
- [8] R. Carballo-Rubio, F. Di Filippo, S. Liberati, C. Pacilio, and M. Visser, *JHEP* **07**, 023, arXiv:1805.02675 [gr-qc].
- [9] R. Carballo-Rubio, F. Di Filippo, S. Liberati, C. Pacilio, and M. Visser, *JHEP* **05**, 132, arXiv:2101.05006 [gr-qc].
- [10] F. S. N. Lobo, *Class. Quant. Grav.* **25**, 175006 (2008), arXiv:0801.4401 [gr-qc].
- [11] G. U. Varieschi and K. L. Ault, *Int. J. Mod. Phys. D* **25**, 1650064 (2016), arXiv:1510.05054 [gr-qc].
- [12] M. Kord Zangeneh, F. S. N. Lobo, and M. H. Dehghani, *Phys. Rev. D* **92**, 124049 (2015), arXiv:1510.07089 [gr-qc].
- [13] A. Övgün, K. Jusufi, and I. Sakalli, *Phys. Rev. D* **99**, 024042 (2019).
- [14] M. Zubair, F. Kousar, and S. Bahamonde, *Eur. Phys. J. Plus* **133**, 523 (2018), arXiv:1712.05699 [gr-qc].
- [15] F. S. N. Lobo and M. A. Oliveira, *Phys. Rev. D* **80**, 104012 (2009).
- [16] C. Boehmer, T. Harko, and F. S. Lobo, *Physical Review D* **85**, 044033 (2012).
- [17] R. Shaikh and S. Kar, *Phys. Rev. D* **94**, 024011 (2016).
- [18] P. Kanti, B. Kleihaus, and J. Kunz, *Phys. Rev. D* **85**, 044007 (2012).
- [19] M. R. Mehdizadeh, M. K. Zangeneh, and F. S. N. Lobo, *Phys. Rev. D* **91**, 084004 (2015).
- [20] H. Maeda and M. Nozawa, *Phys. Rev. D* **78**, 024005 (2008).
- [21] P. Kanti, B. Kleihaus, and J. Kunz, *Phys. Rev. Lett.* **107**, 271101 (2011).
- [22] R. Shaikh, *Phys. Rev. D* **92**, 024015 (2015).
- [23] R. Carballo-Rubio, F. Di Filippo, S. Liberati, C. Pacilio, and M. Visser, *JHEP* **09**, 118, arXiv:2205.13556 [gr-qc].
- [24] A. Bonanno, A.-P. Khosravi, and F. Saueressig, *Phys. Rev. D* **103**, 124027 (2021).
- [25] K. Akiyama *et al.* (Event Horizon Telescope), *Astrophys. J. Lett.* **930**, L12 (2022), arXiv:2311.08680 [astro-ph.HE].
- [26] J. M. Bardeen, presented at GR5, Tiflis, U.S.S.R., and published in the conference proceedings in the U.S.S.R. (1968).
- [27] E. Ayon-Beato and A. Garcia, *Phys. Rev. Lett.* **80**, 5056 (1998), arXiv:gr-qc/9911046.
- [28] E. Ayon-Beato and A. Garcia, *Gen. Rel. Grav.* **31**, 629 (1999), arXiv:gr-qc/9911084.
- [29] E. Ayon-Beato and A. Garcia, *Phys. Lett. B* **464**, 25 (1999), arXiv:hep-th/9911174.

- [30] E. Ayon-Beato and A. Garcia, Phys. Lett. B **493**, 149 (2000), arXiv:gr-qc/0009077.
- [31] E. Ayon-Beato and A. Garcia, Gen. Rel. Grav. **37**, 635 (2005), arXiv:hep-th/0403229.
- [32] I. Dymnikova, Classical and Quantum Gravity **21**, 4417 – 4428 (2004).
- [33] K. Bronnikov, Physical Review D **63**, 10.1103/PhysRevD.63.044005 (2001).
- [34] S. Shankaranarayanan and N. Dadhich, International Journal of Modern Physics D **13**, 1095 – 1103 (2004).
- [35] S. A. Hayward, Phys. Rev. Lett. **96**, 031103 (2006).
- [36] J. L. Synge, Mon. Not. Roy. Astron. Soc. **131**, 463 (1966).
- [37] J. P. Luminet, Astron. Astrophys. **75**, 228 (1979).
- [38] J. M. Bardeen, in Proceedings of the Ecole d’Eté De Physique Theorique: Les Astres Occlus: Les Houches 1972 , 215–240 (1973).
- [39] A. de Vries, Class. Quant. Grav. **17**, 123 (1999).
- [40] K. Hioki and K.-i. Maeda, Phys. Rev. D **80**, 024042 (2009).
- [41] S.-W. Wei and Y.-X. Liu, Journal of Cosmology and Astroparticle Physics **2013** (11), 063.
- [42] A. Abdujabbarov, F. Atamurotov, Y. Kucukakca, B. Ahmedov, and U. Camci, Astrophys. Space Sci. **344**, 429 (2013), arXiv:1212.4949 [physics.gen-ph].
- [43] J. W. Moffat, Eur. Phys. J. C **75**, 130 (2015), arXiv:1502.01677 [gr-qc].
- [44] L. Amarilla and E. F. Eiroa, Phys. Rev. D **85**, 064019 (2012).
- [45] F. Atamurotov, A. Abdujabbarov, and B. Ahmedov, Phys. Rev. D **88**, 064004 (2013).
- [46] R. Roy and S. Chakrabarti, Phys. Rev. D **102**, 024059 (2020), arXiv:2003.14107 [gr-qc].
- [47] B. Rodríguez, J. Chagoya, and C. Ortiz, (2024), arXiv:2403.13062 [gr-qc].
- [48] P. V. P. Cunha and C. A. R. Herdeiro, Gen. Rel. Grav. **50**, 42 (2018), arXiv:1801.00860 [gr-qc].
- [49] V. Perlick and O. Y. Tsupko, Phys. Rept. **947**, 1 (2022), arXiv:2105.07101 [gr-qc].
- [50] A. Lupsasca, D. R. Mayerson, B. Ripperda, and S. Staelens, A Beginner’s Guide to Black Hole Imaging and Associated Tests of General Relativity, in *Recent Progress on Gravity Tests. Challenges and Future Perspectives*, edited by C. Bambi and A. Cardenas-Avendano (2024) pp. 183–237, arXiv:2402.01290 [gr-qc].
- [51] Z. Li and C. Bambi, JCAP **01**, 041, arXiv:1309.1606 [gr-qc].
- [52] A. Abdujabbarov, M. Amir, B. Ahmedov, and S. G. Ghosh, Phys. Rev. D **93**, 104004 (2016), arXiv:1604.03809 [gr-qc].
- [53] Z. Stuchlík and J. Schee, Eur. Phys. J. C **79**, 44 (2019).

- [54] I. Dymnikova and K. Kraav, *Universe* **5**, 163 (2019).
- [55] S. G. Ghosh, M. Amir, and S. D. Maharaj, *Nuclear Physics B* **957**, 115088 (2020).
- [56] A. Uniyal, S. Chakrabarti, M. Fathi, and A. Övgün, *Annals Phys.* **462**, 169614 (2024), arXiv:2309.13680 [gr-qc].
- [57] R. Kumar Walia, *Phys. Rev. D* **110**, 064058 (2024), arXiv:2409.13290 [gr-qc].
- [58] P. Dutta Roy and S. Kar, *Phys. Rev. D* **106**, 044028 (2022), arXiv:2206.04505 [gr-qc].
- [59] S. Kumar, A. Uniyal, and S. Chakrabarti, *Phys. Rev. D* **109**, 104012 (2024), arXiv:2308.05545 [gr-qc].
- [60] V. Perlick, O. Y. Tsupko, and G. S. Bisnovatyi-Kogan, *Phys. Rev. D* **92**, 104031 (2015), arXiv:1507.04217 [gr-qc].
- [61] R. A. Breuer, J. Ehlers, and R. Penrose, *Proceedings of the Royal Society of London. A. Mathematical and Physical Sciences* **370**, 389 (1980), <https://royalsocietypublishing.org/doi/pdf/10.1098/rspa.1980.0040>.
- [62] R. A. Breuer, J. Ehlers, and R. Penrose, *Proceedings of the Royal Society of London. A. Mathematical and Physical Sciences* **374**, 65 (1981), <https://royalsocietypublishing.org/doi/pdf/10.1098/rspa.1981.0011>.
- [63] V. Perlick, *Ray optics, Fermat's principle, and applications to general relativity*, 2000th ed., *Lecture Notes in Physics Monographs* (Springer, Berlin, Germany, 2000).
- [64] J. L. Synge, ed., *Relativity: The General theory* (1960).
- [65] G. S. Bisnovatyi-Kogan and O. Y. Tsupko, *Grav. Cosmol.* **15**, 20 (2009), arXiv:0809.1021 [astro-ph].
- [66] G. S. Bisnovatyi-Kogan and O. Y. Tsupko, *Mon. Not. Roy. Astron. Soc.* **404**, 1790 (2010), arXiv:1006.2321 [astro-ph.CO].
- [67] O. Y. Tsupko and G. S. Bisnovatyi-Kogan, *Phys. Rev. D* **87**, 124009 (2013), arXiv:1305.7032 [astro-ph.CO].
- [68] V. S. Morozova, B. J. Ahmedov, and A. A. Tursunov, *Astrophysics and Space Science* **346**, 513 (2013).
- [69] T. Damour and S. N. Solodukhin, *Phys. Rev. D* **76**, 024016 (2007).